BNL-112013-2016-JA

Visualizing Non-Equilibrium Lithiation of Spinel Oxide via *In Situ* Transmission Electron Microscopy

Kai He[1,*], Sen Zhang[2,*], Jing Li[1], Xiqian Yu[1], Qingping Meng[1], Yizhou Zhu[3], Enyuan Hu[1], Ke Sun[1], Hongseok Yun[2], Xiao-Qing Yang[1], Yimei Zhu[1], Hong Gan[1], Yifei Mo[3], Eric A. Stach[1], Christopher B. Murray[2], and Dong Su[1]

[1]Brookhaven National Laboratory, Upton, New York 11973, USA.

[2]Department of Chemistry, University of Pennsylvania, Philadelphia, Pennsylvania 19104, USA.

[3]Department of Materials Science and Engineering, University of Maryland, College Park, Maryland 20742, USA.

These authors contributed equally to the work. Correspondence and requests for materials should be addressed to C.B.M. (email: cbmurray@sas.upenn.edu) or to D.S. (email: dsu@bnl.gov).

Spinel transition metal oxides are an important class of materials that are being considered as electrodes for lithium-ion batteries, due to their low cost and high theoretical capacity. The lithiation of these compounds is known to undergo a two-step reaction, whereby intercalation and conversion occur in a sequential fashion. These two reactions are known to have distinct reaction dynamics, but it is unclear how the kinetics of these processes affect the overall electrochemical response. Here, we explore the lithiation of nanosized magnetite (Fe_3O_4) by employing a new strain-sensitive, bright-field scanning transmission electron microscopy approach. This method allows direct, real time, high-resolution visualization of how lithiation proceeds along specific reaction pathways. We have found that the initial intercalation process follows a well-known two-phase reaction sequence, whereas further lithiation leads to the coexistence of three distinct phases within single nanoparticles, an observation that has not been reported to date. This process is found to be governed by the competition between energetic barriers to the phase transformations and the overall electrochemical driving force. We use phase field theory to model and describe these non-equilibrium reaction pathways, and to directly correlate the observed phase evolution with the bulk discharge profiles that occur in real batteries.

Keywords: Fe_3O_4 nanoparticles, lithium ion battery, conversion, intercalation, multiple-step, *in situ* TEM

The spinel transition metal oxide family – which includes $LiMn_2O_4$, $Li_4Ti_5O_{12}$, Fe_3O_4, Co_3O_4, Mn_3O_4, among others – is an important group of compounds, and one that sees considerable use as electrode materials in lithium ion batteries.[1-7] Specifically, magnetite (Fe_3O_4) is a promising candidate as an anode material, as it is both inexpensive and non-toxic. Importantly, it also has a high electronic conductivity and can store up to eight Li ions per formula unit, which leads to a high theoretical specific capacity of 926 mAh g^{-1}.[8-20] The structure of Fe_3O_4 is inverse spinel ($(Fe^{3+})_{8a}[Fe^{2+}Fe^{3+}]_{16d}O_4$, denoted by Wyckoff notation), where there are 64 tetrahedral sites in a unit cell (one-eighth of them are 8a sites occupied by 8 Fe^{3+} cations, denoted as), and 32 octahedral sites (half of them are 16d sites occupied by 8 Fe^{2+} and 8 Fe^{3+} cations), leaving behind 56 empty tetrahedral (8b and 48f) sites and 16 empty octahedral (16c) sites in the interstitial space to allow for accommodation of guest Li^+ ions.[17-20] The lithiation of spinel iron oxide was investigated by Thackeray *et al.* using a combination of open-circuit voltage measurements and X-ray diffraction,[16, 17] and they posited that the overall lithiation of Fe_3O_4 follows the reaction equation shown in Eq (1):

$$8\ Li + Fe_3O_4 \rightarrow 4\ Li_2O + 3\ Fe \qquad (1)$$

They suggested that during the initial stage of lithium insertion, the Fe^{3+} cations at tetragonal 8a sites are distorted into the nearby octahedral 16c sites by inserting Li^+ ions into the octahedral 16c sites, which leads to a lattice reconstruction of the spinel structure to form the rocksalt structure, *i.e.*, $(Li^+_xFe^{3+})_{16c}[Fe^{2+}Fe^{3+}]_{16d}O_4$.[16-21] This is an intercalation process, and thus it does not lead to a significant volume change. They proposed that further lithiation triggers destruction of the rocksalt structure along with an extrusion of metallic Fe from the material, which is commonly known as a conversion reaction. During the conversion reaction, the rocksalt structure

transforms into a composite which is composed of both metallic Fe and Li_2O. Critically, this conversion leads to a drastic volume expansion.[9-15]

Fe_3O_4 shows dramatic differences in electrochemical performance as a function of discharge rate ("C rate"), with the intercalation process not readily observed in the discharge voltage profiles.[9-11] These differences cannot be understood from simple consideration of the reaction equation, which describes how these processes occur in an equilibrium condition. In one related example, the positive electrode material $LiFePO_4$ (LFP) exhibits a solid solution transformation at high rates when undergoing an intercalation reaction, specifically when the two-phase transition process is suppressed above a certain overpotential.[22, 23] Thus, it is suggested that for Fe_3O_4 the overall charge-discharge performance depends strongly on the kinetics of specific discharge mechanisms. This in turn determines the realistic redox reaction characteristics that the battery sees in working conditions.

Finally, it is well known that the rate capability of electrodes can be improved by reducing the material size from the micrometer to the nanometer regime. This improvement is due to both the increase in surface area and the reduction of electron/ion diffusion length.[24-26] However, in the case of nanoscale electrodes, the overall kinetics of lithiation are further complicated by local inhomogeneities that can occur in the electrochemical conditions. Besides the presence of both intercalation and conversion reactions, all of these facts underscore the importance of understanding the phase transitions of Fe_3O_4 that occur in non-equilibrium conditions, as it is these parameters that must be optimized when considering spinel-based electrode materials in electrochemical applications.[22]

In this work, we investigate how non-equilibrium intercalation and conversion reactions proceed by studying the lithiation process in real time. X-ray scattering or Mössbauer spectroscopy are most often used to identify the phase transformations that occur in nanosized electrode materials,[16, 19] but these techniques have the disadvantage of providing only average information, and generally they lack the ability to probe reaction kinetics in real time. Critically, it is important to undertake lithiation studies *in situ*, as *ex situ* studies may provide inaccurate information due to changes that may occur during removal of the electrode materials from an actively lithiated condition.[22, 27] In contrast, transmission electron microscopy (TEM) allows direct, real time information to be obtained from structures at the atomic scale. The need for *in situ* observations of this type has been increasingly recognized, and thus there have been many recent reports of the use of *in situ* TEM to study alloying and conversion reactions.[28-38] However, directly visualizing phase transitions that occur during intercalation reactions is challenging because the volume change that occurs during this type of reaction is negligible.[39-42] This prevents the use of standard diffraction contrast imaging techniques. In this work, we have utilized a strain-sensitive bright-field scanning transmission electron microscopy (BF-STEM) imaging technique to overcome this challenge. This approach allows us to observe the phase changes that occur in monodisperse Fe_3O_4 nanoparticles *in situ* during the intercalation reaction, and follow the subsequent conversion reaction directly. By integrating *ex situ* synchrotron X-ray and *in situ* TEM approaches, we capture in detail the mechanisms by which lithiation occurs and relate this directly to the reaction kinetics. Furthermore, we support these observations with both DFT calculations and non-equilibrium phase-field theory to describe the atomistic processes from first principles and phenomenological perspective, respectively. This work highlights the

importance of exploiting advanced TEM techniques to reveal reaction inhomogeneities at the nanoscale.

Results and Discussion

Material structures and electrochemical properties. The as-synthesized Fe_3O_4 nanoparticles are *ca.* 80 nm truncated octahedrons, as shown in Figure 1a and Supplementary Figure S1. Atomic-resolution high-angle annular dark-field (HAADF) STEM images (as in Figure 1b) indicates that the pristine Fe_3O_4 nanoparticles are single-crystalline with the inverse spinel structure ($Fd\bar{3}m$ space group) and terminated with $\{111\}$ crystal planes. In order to characterize the electrochemical performance, voltage profiles at different C-rates (1C, C/10, and C/200, or 926 mA g^{-1}, 92.6 mA g^{-1}, and 4.63 mA g^{-1}, respectively) are shown in Figure 1e. The first discharge capacity is 1080 mAh/g at C/200, and it decreases to 916 mAh/g and 914 mAh/g for C/10 and 1C, respectively, close to the theoretical capacity of 926 mAh/g. The capacity excess in the initial discharge is generally believed due to side reactions involving electrolyte decomposition and formation of solid electrolyte interphases,[43-45] while the following cyclic tests show an excellent rate performance (Figure S2) that is comparable to previous reports.[10-12] After full discharge (lithiation), the electrode materials have changed their structure and morphology dramatically to form a nanocomposite consisting of ultrafine (<5 nm) Fe nanoparticles and an amorphous Li_2O matrix phase (Figure 1c), as confirmed by electron diffraction (Figure 1d). It is noted that two distinct plateaus appear in the C/200 discharge curve, corresponding to the intercalation reaction and conversion reaction, respectively,[13-15, 17] whereas the intercalation plateau is absent from the relatively faster discharge curves at rates of 1C and C/10. This can be due to enhancements in the reaction kinetics that can occur at high discharge current densities (such as voltage polarization). To justify this hypothesis, we employed the galvanostatic

intermittent titration technique (GITT)[46] for a discharge cycle at C/10 to measure the open-circuit voltage (OCV) profile: this reflects the equilibrium redox potentials at different states of charge (SOCs). Figure 1f clearly indicates the voltage polarization between the OCV and regular discharge profile, and confirms the existence of an intercalation plateau which is related to the charge rate. The intercalation process can generally be expressed as Eq (2):

$$x\ \mathrm{Li} + \mathrm{Fe_3O_4}\ (\text{spinel}) \rightarrow \mathrm{Li_xFe_3O_4}\ (\text{rocksalt}) \qquad (2)$$

where x is the lithium content per formula. For an intercalation reaction, x is supposedly between 0 and 2,[16-18] and its upper limit depends on the total amount of lithium ions accommodated at the tetragonal 8a sites.[16, 17] Further lithiation would trigger the conversion reaction. This is also confirmed by high-resolution TEM (HRTEM) imaging of *ex situ* lithiated $Li_xFe_3O_4$ with Li content x = 2, 3, 4, 5, 6, 7, 8 (Figure S3). These HRTEM images and selected area electron diffraction (SAED) patterns show the transition from rocksalt $Li_xFe_3O_4$ to Fe+Li_2O composite in a gradually proceeding fashion. Since the intercalation reaction only involves Li content $x < 2$, it is crucial to focus our study on the first half of the lithiation. To study the intercalation process further, we utilized synchrotron X-ray diffraction (SXRD) to identify the phase changes at various SOCs of x = 0, 0.5, 1, 1.5, 2, 3 and 4, as shown in Figure 1g,h. The series of SXRD patterns show that the electrode materials transfer from spinel structure to rocksalt structure with increasing Li composition (detailed indexing is presented in Supplementary Figure S4). From the enlarged patterns in Figure 1h, we indeed identified the two stable Fe_3O_4 and $LiFe_3O_4$ phases. The nanosized Fe phase that resulted from the conversion reaction cannot be captured by SXRD even up to x = 4: however, its presence was confirmed using TEM (Supplementary Figure S5). These observations clearly indicate that SXRD – due to its lack of sensitivity in detecting nanoscale particles, and its averaging of the overall phase information – is not able to precisely

determine either the initiation of the conversion reaction, or to follow its evolution. Additionally, the absence of an intercalation plateau in the cycling profiles of 1C and C/10 implies that the intercalation process is bypassed at high rates. Although the SXRD results clearly show the existence of a rocksalt intermediate phase which arises from the intercalation reaction, the presence of this phase might also be due to a possible structure relaxation and phase separation that occurs post-mortem. Effects of this type have been reported in LFP system, where *ex situ* characterization is shown to inaccurately describe the reaction processes that are occurring.[21] In addition, the intercalation phase transition can either follow a two-phase model or solid-solution process depending on the details of the reaction kinetics, a process which cannot be resolved from the *ex situ* study. To solve these issues, we have utilized *in situ* electron microscopy approaches to determine which reaction pathways occur in spinel oxide.

Phase evolution by *in situ* electron diffraction. We utilized a dry cell setup for our *in situ* TEM investigation.[36-38] This approach can precisely track the phase evolution at very high spatial resolution. Since there are no liquid organic electrolyte involved in the reactions, to verify the consistency in the phase transitions between the *ex situ* and *in situ* experiments, we tracked the dynamical phase evolution using *in situ* electron diffraction throughout the entire lithiation process, as shown in Figure 2a and Movie 1 The radially integrated intensity profiles from a series of time-sequenced SAED patterns are plotted as a function of lithiation time, with the intensity represented by false colors (Figure 2a). It is obvious that both the position and intensity of the Bragg reflections change as the lithiation proceeds, verifying the overall phase transformation from pristine Fe_3O_4 to the eventual Fe and Li_2O composite (and in the same manner as the *ex situ* results). Using the intensity profiles of Fe_3O_4 (311) and Fe (110) SAED peaks as a measure, the gradual evolution of the phase transformation becomes clear, as depicted

in Figure 2b. It is also worth noting that the Bragg peaks of the Fe_3O_4 phase display a negative shift in reciprocal space (as indicated by arrows in Figure 2a) during the initial stage of lithiation (up to ~1000 s), which corresponds to an increase in the lattice parameter as Li^+ ions are inserted into the Fe_3O_4 lattice (Figure 2c). This lattice parameter increase is quantitatively consistent with the phase transition from Fe_3O_4 to $LiFe_3O_4$, as extracted from our SXRD measurements. After ~1000 s, the lattice expansion becomes more severe, indicating that the subsequent lithiation was dominated by the conversion reaction, as per Eq (3).

$$(8\text{-}x)\ \mathrm{Li} + \mathrm{Li}_x\mathrm{Fe}_3\mathrm{O}_4 \rightarrow 4\ \mathrm{Li}_2\mathrm{O} + 3\ \mathrm{Fe} \qquad (3)$$

Visualization of two-step lithiation by *in situ* STEM. After verifying that the phase transformation occurs using *in situ* SAED, we performed an *in situ* STEM observation to follow how the structure evolves during the entire lithiation process in real space, as shown in Figure 3a and Movie 2. The time-sequenced BF-STEM images record the intensity of the transmitted electrons scattered to lower angles as well as the direct beam (involving the most coherent electron scattering). This signal is strain sensitive and thus enables direct visualization of the small lattice changes that occur during the intercalation process (Figure S6).[47] We show that this is essential observing intercalation reactions in real time. This is contrast to other, more conventional imaging techniques (such as HAADF-STEM, or BF/DF TEM) which does not have the requisite image sensitivity (composition / strain) to directly observe this process. The first intercalation step follows the reaction described in Eq (2) to generate the lithium-inserted $Li_xFe_3O_4$ phase (shown with a lighter contrast). These regions will be further lithiated in the subsequent conversion reaction, which is also accompanied by the extrusion of ultrafine metallic Fe nanoparticles to form a composite with the amorphous Li_2O. For better visualization, we use false colors to distinguish the pristine Fe_3O_4 (red), Li-inserted Fe_3O_4 (blue), and completely

conversion composite (green) phases and their evolution as a function of time. This was also verified using electron energy-loss spectroscopy (EELS) in STEM (Supplementary Figure S7). We note that, under realistic electrochemical environment, the lithiation process shows a non-equilibrium reaction pathway, *i.e.*, the conversion reaction starts to take place before the intercalation completely finishes. This may be likely due to the fact that the diffusion of lithium on the Fe_3O_4 particle surface is faster than that through the lithiated $Li_xFe_3O_4$ phase, which can cause a sufficiently large lithium concentration at the particle surface and thereby trigger the conversion reaction to happen at an early stage (but still after the intercalation reaction). It is obvious that both intercalation and conversion reactions follow a "shrinking-core" mode, proceeding from the outer surface to the inner region.[37] Specifically, the initial intercalation trajectory does not exhibit any preferential directions, in accord with the zigzag Li^+ diffusion paths in three-dimensional (3D) tunnels;[16] whereas the subsequent conversion tends to propagate through the outer facets, *i.e.* {111} planes. As an approximate measure of reaction kinetics, we quantified the projected areas of the three phases versus the lithiation time, displayed in Figure 3b. This figure shows that the propagation speed of the intercalation process is about one order of magnitude faster than the following conversion reaction (Figure 3c). We note that these measurements are from one single particle, where the electrochemical conditions are supposed to be identical. This is consistent with the fact that full conversion needs multiple Li-ion transfers, when compared with the intercalation process. We do not believe this to be an effect resulting from local electrochemical inhomogeneity.

High-resolution TEM characterization. For a fundamental understanding of the intercalated phase, we conducted HRTEM imaging to track the atomic structure changes for both *in situ* and *ex situ* scenarios, as shown in Figure 4. A new phase with the rocksalt structure was

observed *in situ* as Li^+ ions were inserted into the spinel Fe_3O_4 phase (Figure 4a,b). Using two sets of diffraction spots from the fast Fourier transform (FFT, Figure 4a insets), we can separately map the distribution of the spinel (red) and rocksalt (green) phases and thus visualize the propagation of the intercalation front in the reacting Fe_3O_4 crystal (Figure 4c,d). Similarly, in an *ex situ* lithiated sample that was discharged to 0.9 V, we reproduced this result, and found a similar mixture of spinel and rocksalt phases (Figure 4e,g). In the pristine spinel Fe_3O_4 crystals, Fe cations occupy the tetrahedral 8a sites and octahedral 16d sites, which gives the uneven TEM contrast (dim at the diamond center) shown in Figure 4h. Upon lithium insertion, all the cations migrate to the octahedral sites (16c and 16d), leading to a uniform contrast (Figure 4i). This means that the inserted Li ions occupy the 16c sites and also repel the adjacent Fe cations from the 8a to the 16c sites to form $Li_xFe_3O_4$ crystals with the rocksalt structure, with lithium composition up to x= 1. It is also noted from previous reports that the excess Li ions (up to x = 2) could possibly insert into the 8b and 48f sites to form $Li_2Fe_3O_4$ phase without Fe extrusion.[16, 17] However, this particular phase was not experimentally identified from TEM observations. Nevertheless, the intercalation process goes through a two-phase mode and forms an intermediate phase of $Li_xFe_3O_4$.[16-18] Thereafter, the conversion reaction occurs and the $Li_xFe_3O_4$ phase is decomposed into Li_2O and metallic Fe nanocrystals, which can be observed as the speckles in Figure 4b,d. Combining both *in situ* TEM imaging and *ex situ* SXRD results, we now can conclude that the intercalation proceeds in a two-phase "nucleation and growth" manner, resulting in sharp interfacial boundaries between the spinel and rocksalt phases, as expressed in Eq (2).

First principles calculations and phase-field modeling. Density functional theory (DFT) computation has been performed to calculate the voltage profile of the lithiation process

under the thermodynamic equilibrium condition.[48-52] The calculated reaction pathway has multiple voltage plateaus (green dashed curve in Figure 5a) with intermediate phases, such as $LiFeO_2$, Li_2FeO_2 and Li_5FeO_4 (Figure 5b). Given that the $LiFe_3O_4$ is an intermediate phase experimentally observed from SXRD, our DFT calculations also considered a two-step reaction route (red curve in Figure 5a), including the intercalation plateau ($Li + Fe_3O_4 \rightarrow LiFe_3O_4$) and the conversion plateau ($LiFe_3O_4 \rightarrow Li_2O + Fe$). The ground-state $LiFe_3O_4$ structure as illustrated in the inset crystal models of Figure 5a possesses a similar structural framework (*i.e.*, $[Fe]_{16d}O_2$ octahedron) that was inherited from the spinel Fe_3O_4 structure. Consistent with the ground-state $LiFe_3O_4$ structure calculated in the DFT computation, Li ions insert into the octahedral 16c openings, and repel the nearby 8a Fe ions to the other surface-sharing 16c site, which forms the structure identical to that observed in the HRTEM images in Figure 4. In addition, since the octahedral 16c sites are interconnected as a 3D channel, the initial intercalation would proceed in a disordered path, which explains the irregular patterns that are observed during the shrinking-core process in Figure 3. After all of the octahedral 16c sites are filled by Li, the rocksalt lattice becomes more isotropic to the incoming Li ions, which makes the subsequent conversion most likely to propagate across the outline of crystal, again as observed in Figure 3.

Discussion. Given the basics of chemical thermodynamics, the equilibrium lithiation should go through the $LiFe_3O_4$ phase and the subsequent $Fe+Li_2O$ composite in two non-overlapping processes, as proposed by Thackeray *et al.*[16-18] However, our *in situ* results show a clear overlap between the two steps, suggesting that the kinetic effects play an important role during lithiation. On the other hand, the phase-field theory, taking into account the effect of overpotentials, has succeeded in explaining the electrochemical kinetics in lithium-ion battery systems.[53-55] We performed the phase-field simulations in the frame of non-equilibrium

thermodynamics based on the Butler-Volmer equation[55, 56] and the Cahn-Hilliard equation.[23, 57] To simulate the two-step reaction, we constructed a homogeneous free-energy function with three local minima corresponding to the pristine, intercalation, and conversion phases, respectively. In addition, the kinetic contributions from overpotential and volumetric strain have also been included (details in Supplementary Information). The calculated discharge voltage profile is shown in Figure 5c, which qualitatively agrees with the experimental curves in Figure 1e. Figure 5d shows the calculated lithium compositional profiles as a function of time (*x* axis is the dimensionless lithiation direction and *y* axis is the Li composition, details shown in Movie 3). It is found that the formation of $LiFe_3O_4$ phase is predominant in the early stage of lithiation, whereas the conversion reaction initiates immediately afterward and propagates before the complete intercalation, resulting in a mixed lithiation behavior, which is in excellent agreement with the *in situ* STEM observation (Figure 3a). It is well known that the lithiation process (redox stage and reaction speed) in a real battery is heterogeneous due to the fluctuation of local environments.[22] Here we reasonably assume that the local electrochemical conditions are identical for these two reactions within one nanoparticle. By comparing the *in situ* STEM results with phase-field simulation, we believe that the coexistence of Fe_3O_4, $Li_xFe_3O_4$, and $Fe+Li_2O$ phases are due to the competition between the intercalation and conversion reactions. The overall electrochemical kinetics dictates to the applied C-rate, which in turn determines the propagation speeds of the interfaces of $Fe_3O_4/Li_xFe_3O_4$ and $Li_xFe_3O_4/Fe+Li_2O$. Although the reaction speed of intercalation is much faster, the conversion reaction accommodates more Li ions. Therefore, in terms of total lithium insertion capacity, both reactions give important contributions to the overall energy storage rate.

The kinetic lithiation mechanism we proposed here can accommodate the following phenomena which could not be interpreted by the equilibrium theory. (1) As for the discharge profiles in Figure 1e and in literature,[9-11] even the intercalation reaction has not completed, the occurrence of conversion reaction on the surface will reduce the apparent discharge voltage which consequently flattens the first plateau. (2) As for the previous debate on the existence of metallic Fe extrusion,[16-19] due to the kinetic effect, the conversion reaction can happen at the same time of the intercalation reaction, which induces the formation of metallic Fe. For the discharge process at a low rate, the extrusion of metallic Fe is not expected to be observed.

In summary, we have investigated the lithiation mechanism of spinel magnetite using *in situ* strain-sensitive BF-STEM technique as well as DFT and phase-field simulations. By explicit visualization of the two-step intercalation-conversion process of the lithiation in Fe_3O_4 nanocrystals, we found that the initial lithium incalatation leads to formation of the rocksalt $LiFe_3O_4$ phase in a two-phase reaction mode, and the lithium intercalation process significantly overlaps with the subsequent conversion reaction within a single nanoparticle, leading to indistinctness of the discharge profiles. This senario aslo clarifies the mechanism of metallic Fe extrusion during the intercalation process. Our findings have elucidated the ionic occupancy on the atomic level and revealed how rate-dependent kinetic effects can affect the reaction pathway at the single-particle scale. These findings highlight the importance of advanced *in situ* electron microscopy techniques in the field of lithium ion batteries and provide valuable insights to improve the electrochemical performances of other spinel lithium metal oxide cathode materials.

Methods

Materials. Iron acetylacetonate ($Fe(acac)_3$, 99%), oleic acid (OAc, 90%), benzyl ether (BE, 99%), nitrosonium tetrafluoroborate ($NOBF_4$, 95%) were purchased from Sigma-Aldrich and used without any further purification. All solvents, including hexane, isopropanol, toluene, dimethylformamide (DMF), were in ACS reagent grade and were purchased from Fisher Scientific and used without further purification. Nanoparticle synthesis was performed using standard Schlenk techniques.

Sample preparation. The Fe_3O_4 nanoparticles were synthesized by the decomposition of $Fe(acac)_3$ in the presence of oleic acid. In a typical synthesis, 2 mmol of $Fe(acac)_3$ was mixed with 1.28 ml of OAc and 10 ml of BE. The mixture was magnetically stirred and was kept under vacuum at 100 ºC to generate a dark red solution. After evacuation at 100 ºC for 1 hour to remove all impurities and moisture, the system was filled with N_2 and the solution was further heated to 290 ºC at a rate of about 15 °C/min and kept at this temperature for 20 minutes. After cooling to room temperature, the NPs were separated by adding isopropanol, followed by centrifugation (8500 rpm, 5 min). The NPs were further purified by sequential operations of dispersing in hexane, precipitation by adding isopropanol, and centrifugation. The as-synthesized Fe_3O_4 nanoparticles were surface-passivated by OAc which can be ligand-exchanged by $NOBF_4$ according to literature.[58] 0.1 g of $NOBF_4$ was added into 10 ml DMF, resulting in immediately a light green solution. This $NOBF_4$ DMF solution is added to the hexanes solution (10 ml) of Fe_3O_4 NPs (100 mg). The mixture was shaken for 10 min, followed by the addition of 25 ml of toluene. The $NOBF_4$-modified Fe_3O_4 NPs were collected through centrifugation (7000 rpm, 8 min). The Fe_3O_4 NPs after ligand exchange can be solubilized in DMF with sonication. To remove residual organics, The NPs were further purified by two cycles of re-dispersing in DMF

and precipitation by adding toluene-centrifugation. The NPs were either stored in DMF or evacuated at the room temperature overnight to make dry powder for further experiments.

Electrochemical measurements. Composite electrodes were prepared with 80 wt% active material, 10 wt% polyvinylidene fluoride (PVDF) and 10 wt% acetylene carbon black in N-methyl-2-pyrrolidone (NMP) and cast onto copper current collectors. 2032-type coin cells were assembled in an argon-filled glove box using the composite electrode as the positive electrode and Li metal as the negative electrode. A Celgard separator 2400 and 1 M $LiPF_6$ electrolyte solution in 1:1 w/w ethylene carbonate (EC) /dimethyl carbonate (DMC) were used to fabricate coin cells. Battery testing was performed on computer controlled systems (Arbin BT2000 and BioLogic VMP3) at 21°C.

TEM characterization. The *in situ* TEM electrochemical cell was incorporated into a Nanofactory TEM-STM specimen holder, in which Fe_3O_4 nanoparticles dispersed onto a TEM half-grid with amorphous carbon support are analogous to the Fe_3O_4-C composite electrode, Li metal is coated onto a piezo-driven W probe as the counter electrode, with a thin layer of Li_2O formed on Li metal as the solid electrolyte.[36-38] The Li and Fe_3O_4 were loaded onto the holder in an Ar-filled glovebox and then transferred to TEM column using a sealed Ar bag to avoid air exposure. During the *in situ* electrochemical tests, a constant negative DC potential was applied to Fe_3O_4 electrode against the Li source during the lithiation process, and the lithiation processes were captured by real-time imaging in either TEM or STEM mode. We estimated the average discharge current density across the entire particle surface to be 0.017 mA/cm^2. The *ex situ* samples after discharge in coin cells were examined accordingly. The *in situ* BF-STEM measurements were performed on a JEOL 2100F TEM operated at 200 kV. We have used a convergence angle of 12 mrad and a collection angle cut off at ~20 mrad. The high-resolution

STEM imaging and analytical EELS were conducted on a Hitachi HD2700C STEM operated at 200 kV and equipped with a probe aberration corrector (spatial resolution < 1 Å, energy resolution 0.35 eV).

Theoretical calculations. The density functional theory (DFT) calculations were performed using the Vienna Ab initio Simulation Package (VASP) within the projector augmented-wave approach with the Perdew−Burke−Ernzerhof generalized-gradient approximation (GGA). The DFT parameters were consistent with the parameters used in *Materials Project* (MP).[48] A Hubbard U term of 5.3 eV is adopted for Fe^{2+} and Fe^{3+} in accordance with the MP and the previous testing.[51, 52] The ground-state crystal structures of $LiFe_3O_4$ were obtained by enumerating 380 symmetrically distinctive configurations of Li/Fe disordering at the 16c sites using *pymatgen*.[49] Several magnetic orderings in ferromagnetic, antiferromagnetic, and ferrimagnetic structures are tested for iron oxide compounds, such as Fe_3O_4, FeO, $LiFe_3O_4$, and $LiFeO_2$, to identify the lowest energy state (more details provided in Supplementary Information). The voltage plateaus are obtained using the DFT energies of all relevant compounds in the Li-Fe-O ternary space from the MP.[50]

The phase-field simulations were performed using the electrochemistry theory based on non-equilibrium thermodynamics developed by Bazant and coworkers.[53-55] The standard phenomenological model based on the Butler-Volmer equation[55, 56] and the Cahn-Hilliard equation[23, 57] was used for modeling the electrochemical kinetics. A homogeneous free-energy was comprised using piecewise functions of polynomial with continuity and differentiability at the segment points. The overpotential and strain energy are also considered in the simulation. More details are shown in Supplementary Information.

References

1. Poizot, P., Laruelle, S., Grugeon, S., Dupont, L. & Tarascon, J. M. Nano-sized transition-metal oxides as negative-electrode materials for lithium-ion batteries. *Nature* **407**, 496-499 (2000).

2. Tarascon, J. M. & Armand, M. Issues and challenges facing rechargeable lithium batteries. *Nature* **414**, 359-367 (2001).

3. Whittingham, M. S. Lithium Batteries and Cathode Materials. *Chem. Rev.* **104**, 4271-4301 (2004).

4. Goodenough, J. B. & Kim, Y. Challenges for Rechargeable Li Batteries. *Chem. Mater*. **22**, 587-603 (2010).

5. Ferg, E., Gummow, R. J., de Kock, A. & Thackeray, M. M. Spinel Anodes for Lithium-Ion Batteries. *J. Electrochem. Soc*. **141**, L147-L150 (1994).

6. Cabana, J., Monconduit, L., Larcher, D. & Palacin, M. R. Beyond Intercalation-Based Li-Ion Batteries: The State of the Art and Challenges of Electrode Materials Reacting Through Conversion Reactions. *Adv. Mater.* **22**, E170-E192 (2010).

7. Malini, R., Uma, U., Sheela, T., Ganesan, M. & Renganathan, N. G. Conversion reactions: a new pathway to realise energy in lithium-ion battery—review. *Ionics* **15**, 301-307 (2009).

8. Taberna, P. L., Mitra, S., Poizot, P., Simon, P. & Tarascon, J. M. High rate capabilities Fe_3O_4-based Cu nano-architectured electrodes for lithium-ion battery applications. *Nat. Mater*. **5**, 567-573 (2006).

9. Mitra, S., Poizot, P., Finke, A. & Tarascon, J. M. Growth and Electrochemical Characterization versus Lithium of Fe_3O_4 Electrodes Made via Electrodeposition. *Adv. Func. Mater.* **16**, 2281-2287 (2006).

10. Zhou, G. *et al*. Graphene-Wrapped Fe_3O_4 Anode Material with Improved Reversible Capacity and Cyclic Stability for Lithium Ion Batteries. *Chem. Mater*. **22**, 5306–5313 (2010).

11. Ji, L. *et al*. Fe_3O_4 nanoparticle-integrated graphene sheets for high-performance half and full lithium ion cells. *Phys. Chem. Chem. Phys.* **13**, 7170–7177 (2011).

12. Zhang, W. M., We, X. L., Hu, J. S., Guo, Y. G. & Wan, L. J. Carbon Coated Fe_3O_4 Nanospindles as a Superior Anode Material for Lithium-Ion Batteries. *Adv. Func. Mater.* **18**, 3941-3946 (2008).

13. He, Y., Huang, L., Cai, J. S., Zheng, X. M. & Sun, S. G. Structure and electrochemical performance of nanostructured Fe_3O_4/carbon nanotube composites as anodes for lithium ion batteries. *Electrochim. Acta* **55**, 1140-1144 (2010).

14. Xiong, Q. Q. *et al*. Synthesis of Hierarchical Hollow-Structured Single-Crystalline Magnetite (Fe_3O_4) Microspheres: The Highly Powerful Storage versus Lithium as an Anode for Lithium Ion Batteries. *J. Phys. Chem. C* **116**, 6495-6502 (2012).

15. Hariharan, S., Saravanan, K., Ramar, V. & Balaya, P. A rationally designed dual role anode material for lithium-ion and sodium-ion batteries: case study of eco-friendly Fe_3O_4. *Phys. Chem. Chem. Phys.* **15**, 2945-2953 (2013).

16. Thackeray, M. M., David, W. I. F. & Goodenough, J. B. structural characterization of the lithiated iron oxides $Li_xFe_3O_4$ and $Li_xFe_2O_3$ ($0<x<2$). *Mater. Res. Bull.* **17**, 785–793 (1982).

17. Thackeray, M. M. *et al*. Spinel electrodes for lithium batteries – a review. *J. Power Sources* **21**, 1-8 (1987).

18. Thackeray, M. M. Spinel Electrodes for Lithium Batteries. *J. Am. Ceram. Soc.* **82**, 3347-3354 (1999).

19. Fontcuberta, J., Rodriguez, J., Pernet, M., Longworth, G. & Goodenough, J. B. Structural and magnetic characterization of the lithiated iron oxide $Li_xFe_3O_4$. *J. Appl. Phys.* **59**, 1918-1926 (1986).

20. Sivakumar, V., Kumar, S., Ross, C. A. & Shao-Horn, Y. Electrochemical Lithium Insertion of into Iron Oxide Spinel Thin Films and Nanoparticles: Changes in Structure and Magnetic Properties. *ECS Trans.* **2**, 1-11 (2007).

21. Islam, M. S. & Catlow, C. R. A. *J. Solid State Chem.* **77**, 180-189 (1988).

22. Liu, H. *et al*. Capturing metastable structures during high-rate cycling of $LiFePO_4$ nanoparticle electrodes. *Science* **344**, 1252817 (2014).

23. Li, Y. *et al*. Current-induced transition from particle-by-particle to concurrent intercalation in phase-separating battery electrodes. *Nat. Mater.* **13**, 1149-1156 (2014).

24. Arico, A. S., Bruce, P., Scrosati, B., Tarascon, J. M. & van Schalkwijk, W. Nanostructured materials for advanced energy conversion and storage devices. *Nat. Mater*. **4**, 366-377 (2005).

25. Jamnik, J. & Maier, J. Nanocrystallinity effects in lithium battery materials: Aspects of nano-ionics Part IV. *Phys. Chem. Chem. Phys.* **5**, 5215-5220 (2003).

26. Malik, R., Burch, D., Bazant, M. & Ceder, G. Particle Size Dependence of the Ionic Diffusivity. *Nano Lett*. **10**, 4123-4127 (2010).

27. Malik, R., Zhou, F. & Ceder, G. Kinetics of non-equilibrium lithium incorporation in $LiFePO_4$. *Nat. Mater*. **10**, 587–590 (2011).

28. Huang, J. Y. *et al*. In Situ Observation of the Electrochemical Lithiation of a Single SnO_2 Nanowire Electrode. *Science* **330**, 1515-1520 (2010).

29. Liu, X. H. *et al*. In situ atomic-scale imaging of electrochemical lithiation in silicon. *Nat. Nanotechnol.* **7**, 749-756 (2012).

30. Liu, Y. *et al*. In Situ Transmission Electron Microscopy Observation of Pulverization of Aluminum Nanowires and Evolution of the Thin Surface Al_2O_3 Layers during Lithiation-Delithiation Cycles. *Nano Lett*. **11**, 4188-4194 (2011).

31. McDowell, M. T. *et al*. Studying the Kinetics of Crystalline Silicon Nanoparticle Lithiation with In Situ Transmission Electron Microscopy. *Adv. Mater*. **24**, 6034-6041 (2012).

32. McDowell, M. T. *et al*. In Situ Observation of Divergent Phase Transformations in Individual Sulfide Nanocrystals", *Nano Lett.* **15**, 1264-1271 (2015).

33. Gu, M. *et al*. *In Situ* TEM Study of Lithiation Behavior of Silicon Nanoparticles Attached to and Embedded in a Carbon Matrix. *ACS Nano* **6**, 8439-8447 (2012).

34. Gu, M. *et al*. Probing the Failure Mechanism of SnO_2 Nanowires for Sodium-Ion Batteries. *Nano Lett.* **13**, 5203-5211 (2013).

35. Nie, A. *et al*. Atomic-Scale Observation of Lithiation Reaction Front in Nanoscale SnO_2 Materials. *ACS Nano* **7**, 6203-6211 (2013).

36. He, K. *et al*. Sodiation via Heterogeneous Disproportionation in FeF_2 Electrodes for Sodium-Ion Batteries. *ACS Nano* **8**, 7251-7259 (2014).

37. He, K. *et al*. Transitions from Near-Surface to Interior Redox upon Lithiation in Conversion Electrode Materials. *Nano Lett.* **15**, 1437-1444 (2015).

38. He, K. *et al*. Sodiation Kinetics of Metal Oxide Conversion Electrodes: a Comparative Study with Lithiation. *Nano Lett.* **15**, 5755-5763 (2015).

39. Zhu, Y. *et al*. In Situ Atomic-Scale Imaging of Phase Boundary Migration in $FePO_4$ Microparticles During Electrochemical Lithiation. *Adv. Mater*. **25**, 5461-5466 (2013).

40. Niu, J. *et al*. In situ observation of random solid solution zone in $LiFePO_4$ electrode. *Nano Lett.* **14**, 4005-4010 (2014).

41. Sun, Y. *et al*. Direct atomic-scale confirmation of three-phase storage mechanism in $Li_4Ti_5O_{12}$ anodes for room-temperature sodium-ion batteries. *Nat. Commun*. **4**, 1870 (2013).

42. Lu, X. *et al*. Lithium storage in $Li_4Ti_5O_{12}$ spinel: The full static picture from electron microscopy. *Adv. Mater*. **24**, 3233-3238 (2012).

43. Laruelle, S. *et al*. On the Origin of the Extra Electrochemical Capacity Displayed by MO/Li Cells at Low Potential. *J. Electrochem. Soc.* **149**, A627-A634 (2002).

44. Ponrouch, A., Taberna, P. L., Simon, P. & Palacin, M. R. On the origin of the extra capacity at low potential in materials for Li batteries reacting through conversion reaction. *Electrochimica Acta* **61**, 13-18 (2012).

45. Hu, Y. Y. *et al*. Origin of additional capacities in metal oxide lithium-ion battery electrodes. *Nat. Mater.* **12**, 1130-1136 (2013).

46. Weppner, W., & Huggins, R. A. Determination of the Kinetic Parameters of Mixed-Conducting Electrodes and Application to the System Li_3Sb. *J. Electrochem. Soc*. **124**, 1569-1578 (1977).

47. Pennycook, S. J. & Nellist, P. D. *Scanning Transmission Electron Microscopy Imaging and Analysis*. 97-101, (Springer Science & Business Media, 2011).

48. Jain, A. *et al*. A high-throughput infrastructure for density functional theory calculations. *Comp. Mater. Sci*. **50**, 2295–2310 (2011).

49. Ong, S. P. *et al*. Python Materials Genomics (pymatgen): A Robust, Open-Source Python Library for Materials Analysis. *Comp. Mater. Sci*. **68**, 314–319 (2013).

50. Jain, A. *et al*. The Materials Project: A materials genome approach to accelerating materials innovation. *APL Mater*. **1**, 011002 (2013).

51. Jain, A. *et al*. Formation enthalpies by mixing GGA and GGA+U calculations. *Phys. Rev. B* **84**, 045115 (2011).

52. Wang, L., Maxisch, T. & Ceder, G. Oxidation energies of transition metal oxides within the GGA+U framework. *Phys. Rev. B* **73**, 195107 (2006).

53. Bazant, M. Z. Theory of Chemical Kinetics and Charge Transfer based on Nonequilibrium Thermodynamics. *Acc. Chem. Res*. **46**, 1144-1160 (2013).

54. Bai, P., Cogswell, D. A. & Bazant, M. Z. Suppression of Phase Separation in $LiFePO_4$ Nanoparticles During Battery Discharge. *Nano Lett*. **11**, 4890-4896 (2011).

55. Biesheuvel, P. M., van Soestbergen, M. &Bazant, M. Z. Imposed currents in galvanic cells. *Electrochimica Acta* **54**, 4857-4871 (2009).

56. Newman, J. *Electrochemical Systems, 2nd Ed*. (Prentice Hall, 1991).

57. Cahn, J. W. & Hilliard, J. E. Free Energy of a Nonuniform System. I. Interfacial Free Energy. *J. Chem. Phys*. **28**, 258-267 (1958).

58. Dong, A. *et al*. A Generalized Ligand-Exchange Strategy Enabling Sequential Surface Functionalization of Colloidal Nanocrystals. *J. Am. Chem. Soc.* **133**, 998–1006 (2011).

Acknowledgements

This research used resources of the Center for Functional Nanomaterials, which is a U.S. DOE Office of Science Facility, at Brookhaven National Laboratory under Contract No. DE-SC0012704. X.Y. and X.-Q.Y. were supported by the U.S. DOE, the Assistant Secretary for Energy Efficiency and Renewable Energy, Office of Vehicle Technologies under Contract No. DE-SC00112704. The authors acknowledge the technical support by Dr. Wenqian Xu from Beamline 17-BM-B of Advanced Photon Source at Argonne National Laboratory. S.Z., H.Y. and C.B.M. acknowledge the support of MRSEC award No. DMR-1120901. S.Z. also acknowledges the support of the NatureNet Science Fellowship. Q.M. and Yimei Z. were supported by DOE/BES, Division of Materials Science and Engineering, under Contract No. DE-SC0012704. Work by J. L. and E. A. S. are supported as part of the Center for Mesoscale Transport Properties, an Energy Frontier Research Center supported by the U.S. Department of Energy, Office of Science, Basic Energy Sciences, under award #DE-SC0012673. Yizhou Z. and Y.M. acknowledge the support of the Minta Martin award at University of Maryland, and the computational resources from Extreme Science and Engineering Discovery Environment (XSEDE) supported by National Science Foundation Grant No. TG-DMR130142 and from University of Maryland supercomputing resources. We thank Dr. Peng Bai for helpful discussion on phase-field simulaitons.

Author contributions

K.H., S.Z., D.S. and C.B.M conceived and designed the experiments. K.H., D.S. and J.L. performed *in situ* and *ex situ* TEM experiments. S.Z., H.Y., and C.B.M. synthesized the Fe_3O_4 samples. X.Y., X.-Q.Y., J.L., K.S. and H.G. conducted electrochemical tests. Yizhou Z. and Y.M.

performed DFT simulation. Q.M. performed phase-field simulation. K.H. prepared the figures and wrote the manuscript with D.S., S.Z., E.A.S., Yimei Z. and C.B.M. D.S. supervised the project. All the authors participated in discussion of the results.

Additional information

Supplementary Information accompanies this paper at

http://www.nature.com/naturecommunications

Competing financial interests: The authors declare no competing financial interests.

Reprints and permissions information is available online at

http://npg.nature.com/reprintsandpermission

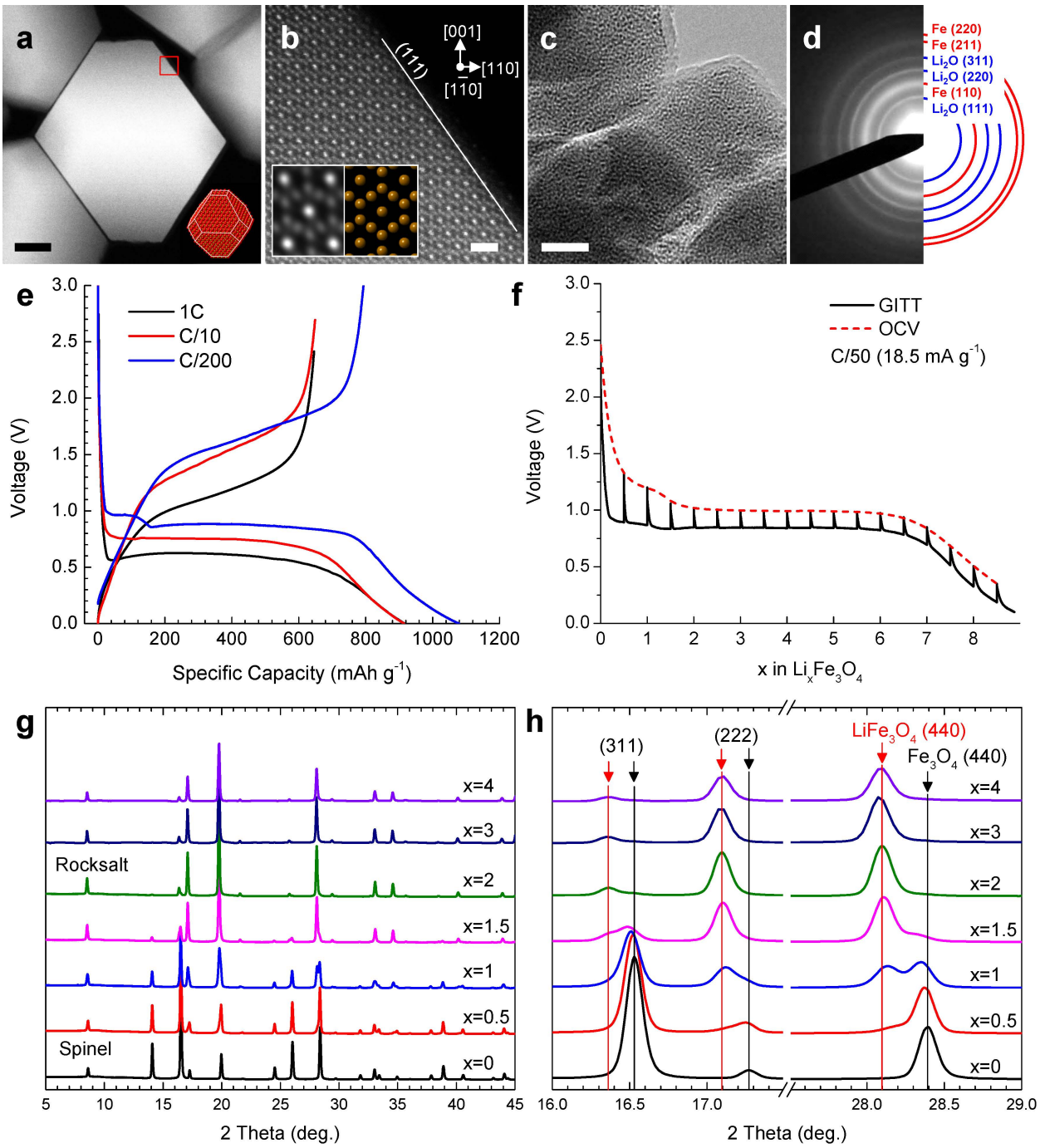

Figure 1 | Electrode materials and electrochemical performance. (a) STEM image of the pristine Fe_3O_4 single crystals. Inset showing the crystals in the truncated octahedral shape. (b) High-resolution HAADF-STEM image showing spinel structure along [1-10] zone axis. Inset showing enlarged STEM image compared to the atom

model. (c) TEM image and (d) SAED pattern of the fully lithiated electrode, confirming the nanocomposite of Fe nanocrystals in amorphous Li_2O matrix. Scale bars, (a, c) 20 nm; (b) 1nm. (e) First-cycle charge/discharge profiles of coin-cell batteries at rates of 1C, C/10, and C/200 (*i.e.*, 926 mA g^{-1}, 92.6 mA g^{-1}, and 4.63 mA g^{-1}). (f) GITT and OCV profiles in the first discharge cycle measured at C/50 (18.5 mA g^{-1}). (g) SXRD patterns of $Li_xFe_3O_4$ at various SOCs (x = 0, 0.5, 1, 1.5, 2, 3, 4). (h) Enlarged SXRD patterns showing detailed peak shifts of (311), (222) and (440) reflections. Fe_3O_4 and $LiFe_3O_4$ phases are marked by black and red arrows. X-ray wavelength is 0.72768 Å.

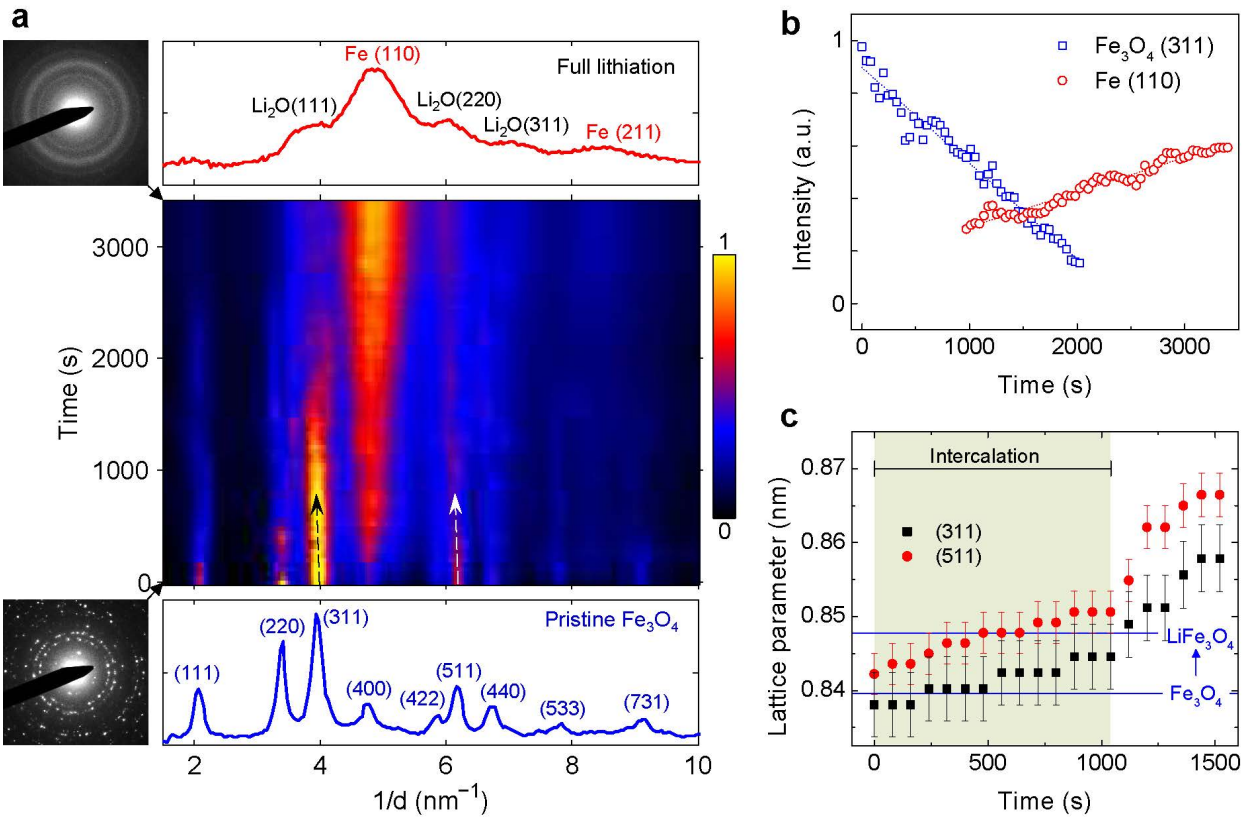

Figure 2 | Phase evolution probed by *in situ* electron diffraction. (a) Electron diffraction intensity profile (the color map in the middle) as a function of reaction time during an *in situ* lithiation of Fe_3O_4 nanoparticles (see Movie 1). The SAED patterns and corresponding radially integrated intensity profiles obtained at pristine (0s) and fully lithiated (3400s) states are shown below and above the color map, respectively. Arrows indicate diffraction peak shift towards a lower value in the reciprocal space. The sample was lithiated at a rate of ~980 mA g^{-1}. (b) Intensity profiles of Fe_3O_4 (311) and Fe (110) Bragg reflections during the lithiation, indicating the phase evolution of Fe_3O_4 and Fe. (c) Lattice parameter measured from Fe_3O_4 (311) and (511) reflections showing an incremental shift as a function of lithiation time, which quantitatively agrees with the SXRD results. Blue lines indicate lattice parameters of Fe_3O_4 and $LiFe_3O_4$ measured by SXRD in Figure 1g.

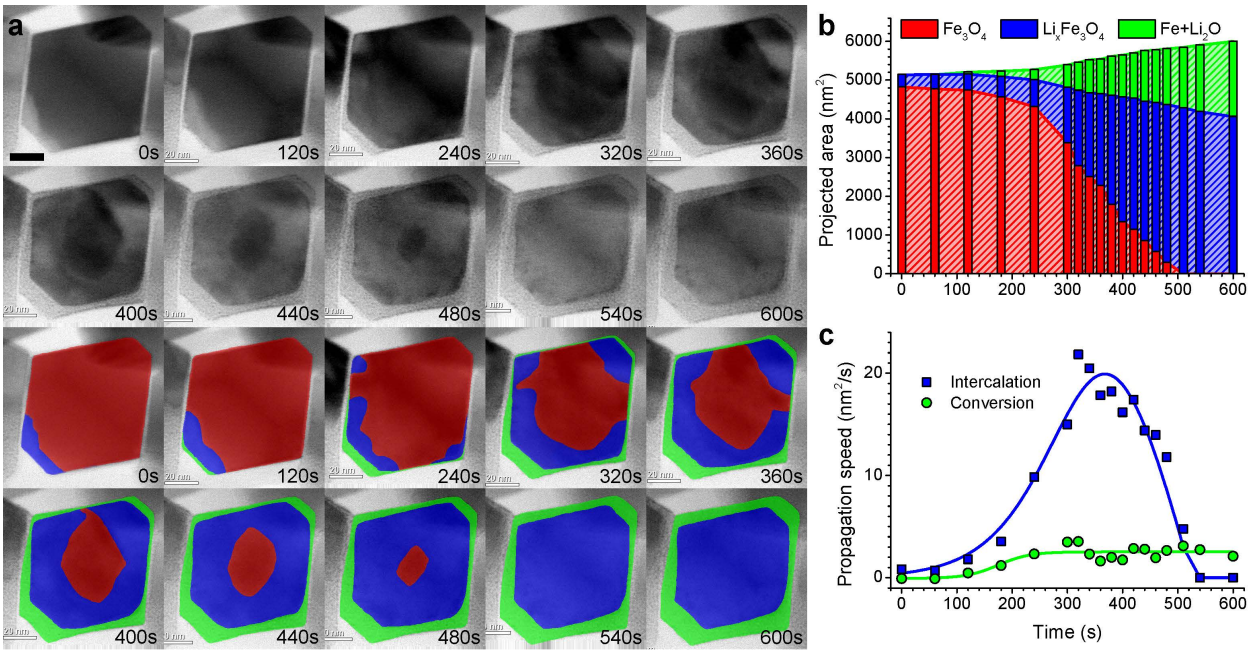

Figure 3 | *In situ* observation of two-step phase transformation during lithiation process. (a) BF-STEM image series showing phase evolution upon lithiation. The overlaid false colors indicate different phases: pristine Fe_3O_4 (red), Li-inserted $Li_xFe_3O_4$ (blue), and $Fe+Li_2O$ composition after conversion (green). Scale bar, 20 nm. The sample was lithiated at a rate of ~2700 mA g^{-1}. (b) Projected areas of the three phases as a function of time. (c) Propagation speed of intercalation and conversion as a function of time.

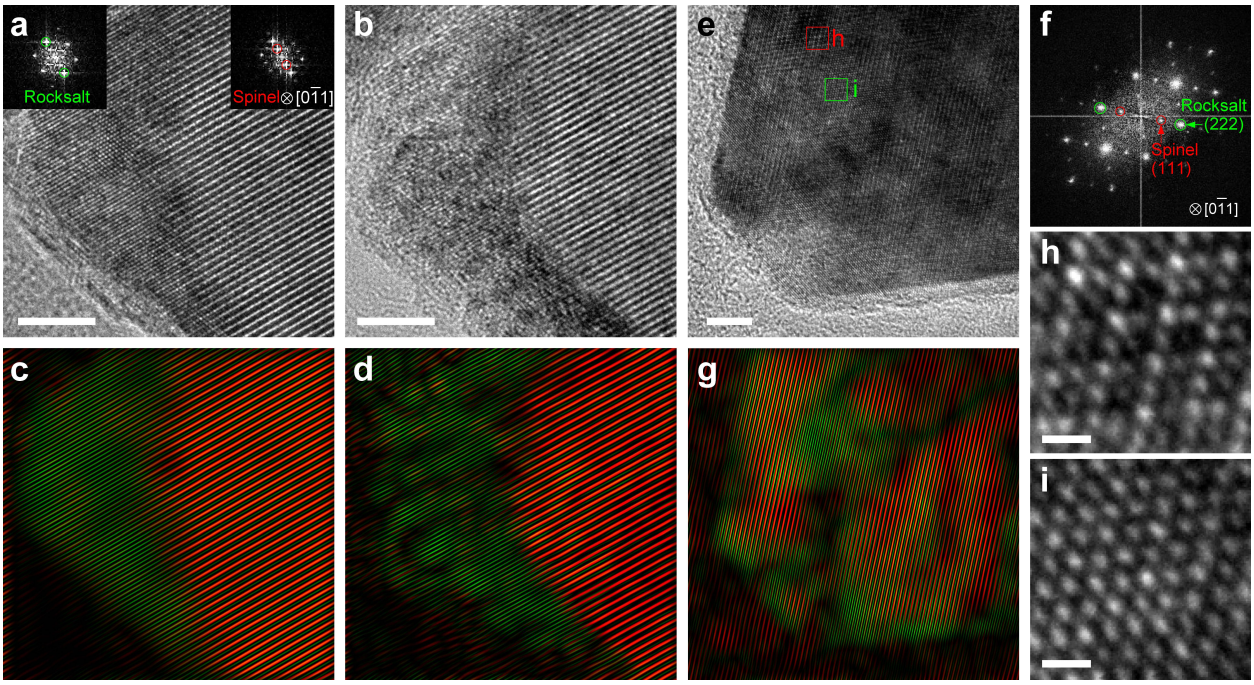

Figure 4 | Atomic structural evolution of phase transformation from spinel to rocksalt structures. (a, b) HRTEM images of a Fe_3O_4 single crystal showing the spinel and rocksalt phases during *in situ* lithium intercalation. Insets showing the FFT of the spinel (top-right) and rocksalt (top-left) structures along [0-11] zone axis. (e) HRTEM image of a partially lithiated Fe_3O_4 single crystal from *ex situ* lithiation. (f) The FFT of (e). (h, i) The enlarged HRTEM images of boxed regions in (e) showing spinel and rocksalt structures, respectively. (c, d, g) Filtered images of (a, b, e) using two sets of spinel (red) and rocksalt (green) diffraction spots to indicate the corresponding phase distribution. The samples were lithiated at ~150 mA g^{-1} for *in situ* lithiation, and 92.6 mA g^{-1} for *ex situ* lithiation. Scale bars, (a, b, e) 5 nm; (h, j) 5 Å.

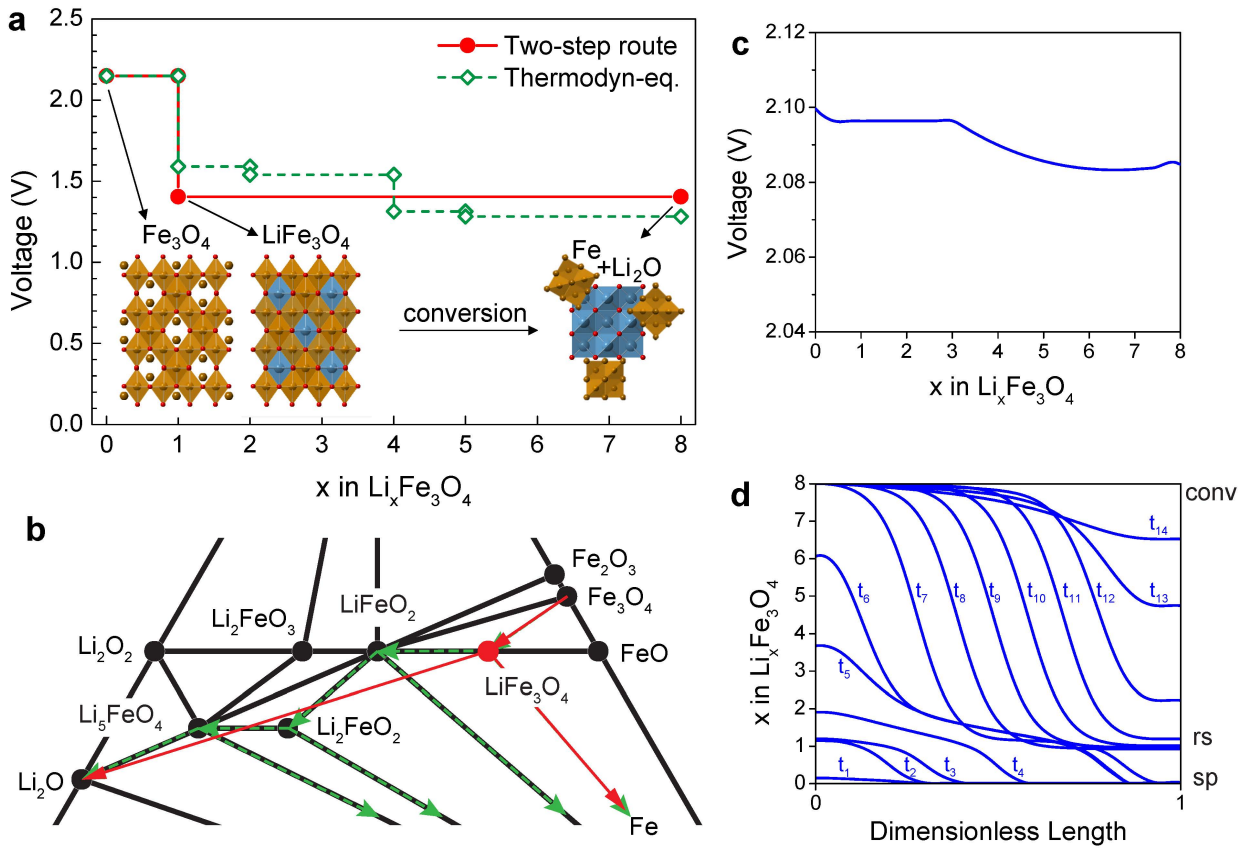

Figure 5 | DFT and phase-field simulations of lithiation process in Fe_3O_4 crystals. (a) The voltage profiles as a function of Li composition (x = 1–8) calculated by DFT showing both thermodynamic equilibrium (green lashed lines) and two-step reaction (red solid lines) routes for an entire lithiation process. The inset models showing crystal structures of Fe_3O_4 and $LiFe_3O_4$ phases during the intercalation process, and a schematic of Li_2O plus metallic Fe after the complete conversion reaction. Color spheres representing Fe (yellow), Li (blue), and O (red). (b) Li-Fe-O phase diagram with overlaid arrow lines showing lithiation pathways through thermodynamic equilibrium multistep route (green dashed lines) or experimentally observed two-step route (red solid lines). (c) Discharge voltage profiles calculated from the phase-field modeling. (d) Li composition profiles along one-dimensional length as a function of reaction time simulated by the phase-field theory (also see Movie 3). The time intervals are uniform between adjacent time stamps.